RIVER RESEARCH AND APPLICATIONS
River Res. Applic. **30**: 905–924 (2014)

EVALUATING SHALLOW-WATER BATHYMETRY FROM THROUGH-WATER TERRESTRIAL LASER SCANNING UNDER A RANGE OF HYDRAULIC AND PHYSICAL WATER QUALITY CONDITIONS

M.W. SMITH[a]* AND D. VERICAT[b,c,d]
[a] *School of Geography, University of Leeds, Leeds, UK*
[b] *Fluvial Dynamics Research Group (RIUS), Department of Environment and Soil Sciences, University of Lleida, Lleida, Catalonia, Spain*
[c] *Forestry and Technology Centre of Catalonia, Solsona, Catalonia, Spain*
[d] *Institute of Geography and Earth Sciences, Aberystwyth University, Wales, UK*

ABSTRACT

The fine-scale structure of the water–sediment boundary in fluvial environments is dynamic and complex, influencing near-bed flows, sediment transport and instream ecology. However, accurate high-resolution surveying of marginally or partially inundated areas of river channels is problematic. Previous work has shown that terrestrial laser scanning (TLS) through relatively shallow-water columns using standard green-wavelength equipment introduces errors of <5 mm in a static, clear water column. This paper presents seven laboratory and field tests of through-water TLS under variable flow velocities, depths, suspended sediment concentrations, water colour levels and scan ranges. Flow velocity decreased point accuracy only for supercritical flows, whereas point density decreased as a function of both water depth and suspended sediment concentration. A similar point return threshold was observed for water colour variations with no grains in suspension. Conversely, point precision and accuracy were a function of suspended sediment concentration alone (a threshold of $0.11\,\mathrm{g\,L^{-1}}$ was observed). Field tests showed larger errors (<10 mm) and lower point precisions. A clear-water depth-penetration limit of 0.68 m was identified. Fluvial bathymetry acquired from through-water TLS is presented for a gravel/boulder bed reach. Despite observed limits, these experiments demonstrate that our approach provides centimetre-resolution bathymetry and sub-aerial survey in an integrated dataset without the need for the following: (i) additional financial resources; (ii) concurrent depth measurements; or (iii) extra field effort for bathymetry acquisition, thereby enabling regular surveys to characterize the fine-scale structure of channel beds and to constrain the geomorphic effect of individual flood events. Copyright © 2013 John Wiley & Sons, Ltd.

KEY WORDS: terrestrial laser scanning; bathymetry; roughness; fluvial geomorphology

Received 30 November 2012; Revised 19 April 2013; Accepted 03 June 2013

INTRODUCTION

River management activities demand increasingly high-resolution topographic datasets of both exposed and submerged channel boundaries. The development of computationally efficient hydraulic algorithms alongside relaxed computational constraints presents the opportunity of driving flood inundation models using decimetre-scale topographic data (Mandlburger *et al*., 2009; Fewtrell *et al*., 2011; Sampson *et al*., 2012). Similarly, fine-scale computational fluid dynamics models demand high-resolution topographic data at the water–sediment boundary (Lane *et al*., 2004; Hardy *et al*., 2005). Developing reach-scale distributed sediment budgets using the morphological method requires repeat topographic surveys (Ashmore and Church, 1998; Brasington *et al*., 2000; Lane *et al*., 2003; Wheaton *et al*., 2010; Milan *et al*., 2011; Fuller and Basher, 2012) and can be used alongside flow data to evaluate the interactions between sediment transport, topographic change and flow hydraulics. Meanwhile, resource managers require extensive high-resolution habitat maps that rely partially on topographic datasets (Hauer *et al*., 2009; 2011; Raineault *et al*., 2012). At the fine scale, understanding the effect of surface roughness on near-bed flows (Smith *et al*., 2007; Lacey and Roy, 2008), sediment transport (Petit *et al*., 2005) and ecological processes (Lancaster *et al*., 2006; Gibbins *et al*., 2010; Hauer *et al*., 2012) requires high-resolution surface models of channel beds at the grain scale. Both terrestrial and bathymetric lidar are capable of meeting this demand, especially as hardware becomes both more advanced and affordable and developments in point cloud processing facilitate the generation of useful data products (e.g. Brasington *et al*., 2012; Rychkov *et al*., 2012).

Reach-scale digital elevation models are typically acquired using airborne lidar (Hauer *et al*., 2009; Höfle and Rutzinger, 2011), digital photogrammetry (Lane, 2000; Westaway *et al*., 2000) or, at a higher resolution, terrestrial laser scanners (TLS; Milan *et al*., 2007). Although each of these technologies

---

*Correspondence to: M.W. Smith, School of Geography, University of Leeds, Leeds, UK, LS2 9JT.
E-mail: m.w.smith@leeds.ac.uk

provides a different range of resolutions and accuracies that could be acceptable in relation to the spatial scale of the survey or the landform characterized, all are subject to relatively large uncertainties when surveying submerged riverbed topography (Brasington *et al*., 2003; Milan *et al*., 2007). Yet, inundated areas that remain submerged at the lowest flow levels are most likely to be the focus of geomorphic activity (in comparison with exposed surfaces on gravel bars) and, as they remain perennially submerged, form important habitats for benthic invertebrates and fish (Gibbins *et al*., 2010).

Conversely, the use of total stations (Milne and Sear, 1997) or real-time kinematic differential global positioning systems (Wheaton *et al*., 2010; Fuller and Basher, 2012) is relatively unaffected by the presence of surface water (within field safety constraints) and provides higher-accuracy bathymetry. Despite the time-consuming nature and low resolution of these survey methods for large spatial coverage (typically < 1 point per square metre), total-station bathymetric measurements are often fused with airborne lidar surveys of exposed surfaces for a complete topographic model of a river corridor (Hauer *et al*., 2011; Vetter *et al*., 2011). Alternatively, submerged zone bathymetry can be obtained through optical–empirical reflectance depth monitoring (Winterbottom and Gilvear, 1997; Westaway *et al*., 2003; Fonstad and Marcus, 2005; Carbonneau *et al*., 2006; Legleiter *et al*., 2009; Williams *et al*., 2011). This technique provides reach-scale coverage and has been used extensively; however, it also requires the survey of concurrent depths and is limited to reasonably clear-water conditions (Gao, 2009).

Bathymetric green airborne lidar (Guenther *et al*., 2000; Hilldale and Raff, 2008; Bailly *et al*., 2010) is thought to have a maximum turbidity-dependent penetration depth of up to 60 m (Wang and Philpot, 2007; Gao, 2009) with average errors as low as 0.10 m (McKean *et al*., 2009). However, the high operating cost and coarse sampling interval of several metres render this method inappropriate for many studies, especially those requiring regular multi-temporal accurate surveys. Bathymetric sonar (Raineault *et al*., 2012) has also been used, although logistical difficulties relating to navigation and clearance depths preclude reliable vessel-based surveys in shallow areas (<0.20 m) typical of many upland rivers.

Resolving grain-scale topographic variability requires higher-resolution datasets. Investigation of fine-scale sedimentary structures in submerged zones is necessary to understand roughness effects on both hydraulic and ecological processes. At finer scales, stereo-photogrammetry (Butler *et al*., 1998) and TLS (Hodge *et al*., 2009) have been used to acquire sub-centimetre-resolution topographic models of exposed fluvial sediments. Butler *et al*. (2002) applied close-range digital photogrammetry to submerged gravel patches, although acquiring both surface and bed control points is problematic in deeper water. Recently, Smith *et al*. (2012) demonstrated the potential of through-water TLS for high-resolution surveys of submerged surfaces. The through-water patch-scale method is relevant for ecological applications because laboratory-based reproductions of natural gravel surfaces (Buffin-Bélanger *et al*., 2003) cannot fully represent inter-particle surfaces and the permeable hyporheic zone observed in the field (Rice *et al*., 2010). Thus, through-water TLS enables evaluation of invertebrate behaviour and the dynamic response of instream habitat availability to different flow regimes in a more natural, undisturbed field setting.

Smith *et al*. (2012) demonstrated that such patch-scale scans could be acquired in field situations and embedded seamlessly into reach-scale TLS surveys of exposed surfaces (Figure 1). Field and laboratory validations under ideal conditions of static, clear-water bodies showed that through-water scans (using green-wavelength time-of-flight TLS) were accurate to within ~5 mm (Smith *et al*., 2012). Furthermore, no detrimental effect on point precision was observed through a water depth of at least 200 mm. Before through-water TLS was undertaken in the field, Smith *et al*. (2012) created a static, clear-water body using a small dam; however, such ideal survey conditions may not always be achievable. Therefore, greater knowledge of the conditions within which through-water TLS can be applied, and the resulting uncertainties expected with each condition, opens up the potential for through-water TLS to be used within laboratory experiments where draining water is impractical or time-consuming or in the field to survey short river reaches. In the latter case, degradation of point accuracy, precision and resolution would be expected; however, this may fall within acceptable levels depending on the purpose of the survey. Given efficiency gains from obtaining sub-aerially exposed and submerged topography in a single integrated dataset, the possibility is worthy of investigation.

Following the preliminary work by Smith *et al*. (2012), seven new experiments are presented here, each with a different specific objective (Table 1) to report the conditions within which through-water TLS can be applied. Laboratory experiments (LEs) were conducted to evaluate the limits of through-water TLS under controlled conditions, whereas field experiments (FEs) aim to evaluate the method at broader scales, where it is anticipated that point accuracy, precision and density will be degraded, but nevertheless, through-water TLS may provide a useful approximation of the riverbed with no hydraulic manipulation.

Flowing water or wind stress will create an uneven water surface, which may influence the density and accuracy of bottom returns. Full-waveform lidar (Mallet and Bretar, 2009) or two-beam lidar systems (Guenther *et al*., 2000) permit accurate mapping of the water surface, although such systems are not always available. For reasonably steady flows in laboratory conditions, Legout *et al*. (2012) seeded water with low concentrations of titanium oxide to provide

DOI: 10.1002/rra

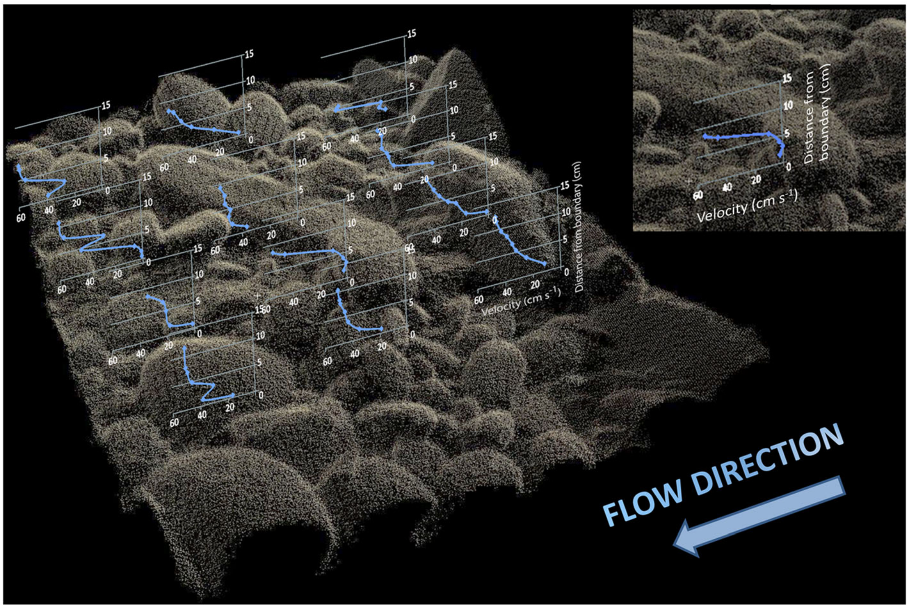

Figure 1. Oblique view of through-water terrestrial laser scanning-derived point cloud with acoustic Doppler velocimeter velocity profiles overlaid (y-axes correspond to profile locations). Inset: magnification of the central velocity profile and surrounding submerged topography where the effects of individual gravels on the velocity profile can be observed. The point cloud was acquired in the Ribera Salada (Catalan Pre-Pyrenees) from multiple scanning directions. Adapted from Smith *et al.* (2012, p. 420). This figure is available in colour online at wileyonlinelibrary.com/journal/rra

sufficient surface reflectance to map water surface elevations using laser scanning systems. Assuming steady flow, rapid water surface scans could be acquired after through-water scanning is complete; however, this would be inappropriate in the field.

Moreover, absorption and scattering by turbid or coloured water will result in attenuation of the laser, limiting the applicability of through-water TLS (as seen with airborne bathymetric lidar; Guenther *et al.*, 2000). Light attenuation in natural water bodies is thought to be more affected by particulate components than soluble components (James *et al.*, 2002; Karlsson *et al.*, 2009); yet in large concentrations as found in areas draining peatlands, for example, soluble substances may attenuate the laser and limit the ability to acquire bed returns.

Within this context, the aim of this paper is to expand the validation of the through-water TLS technique through the following: (i) examining the effects of flow velocity, wind speed, suspended sediment concentration (SSC) and water colour on the accuracy, precision and resolution of through-water TLS under controlled laboratory conditions; and (ii) undertaking field tests to establish errors observed in typical field situations and establish flow depth, velocity and range limits of the method. Finally, a reach-scale demonstration of through-water TLS is presented briefly.

METHODS

Laboratory and field experiments were conducted with a Leica ScanStation TLS and Leica ScanStation C10, respectively. Both scanners use a 532-nm pulsed laser, which can penetrate water and is well suited to through-water applications. The effects observed in this study are applicable to

Table I. Summary of field and laboratory experiments

Setting	Experiment	Variable	Range investigated	Scan system
Laboratory	LE1	Flow velocity	0-0.61 m s^{-1}	Leica ScanStation
	LE2	Water surface roughness (surface wind speed)	0-6.0 m s^{-1}	
	LE3	Suspended sediment concentration	0-0.31 g L^{-1}	
	LE4	Water colour (absorbance)	0-0.45	
Field	FE1	Accuracy in field conditions	Dry versus submerged	Leica ScanStation C10
	FE2	Maximum flow depth/velocity	0-0.9 m/0.51-1.33 m s^{-1}	
	FE3	Survey range	2-14 m	

FE, field experiment; LE, laboratory experiment.

other green-wavelength TLS systems; those using infrared laser beams are unsuitable for through-water applications because of the heavy absorption of infrared wavelengths by water. The scan rate of the Leica ScanStation is 4000 points per second whereas the C10 can obtain a maximum of 50 000 points per second. Both scanners have a maximum range of 300 m, and stated precisions are 6 mm for position, 4 mm for distance and 60 µrad for angles (one standard deviation σ) (Leica Geosystems, 2007, 2011). Minimum point spacing is 1.2 mm (or <1 mm for the C10), although in practice, the achievable resolution is limited by the laser footprint size at a given range. The point spread function is 4 mm over ranges up to 50 m, although a greater spread will be observed through the water column.

The typically oblique survey angle of TLS equipment necessitates accurate correction for refraction at the air–water interface. Where no refraction correction is applied, vertical errors of through-water points are similar in magnitude to the reported flow depth (Milan *et al*., 2007). An overview of the refraction correction is presented in Figure 2. For specific details, see Smith *et al*. (2012). Point cloud data are transformed from Cartesian to polar co-ordinates, which simplifies the correction procedure. Correction for refraction requires the specification of four parameters: the refractive index n, the water surface height z_w in the local TLS survey co-ordinates and the horizontal and vertical offsets of the point of laser emission from the arbitrary origin of the local TLS co-ordinate system (z_{off} and x_{off}, respectively).

The value of the refractive index n determines the relationship between the angle of incidence θ_a and angle of refraction θ_w at the water surface according to Snell's law,

$$\frac{\sin\theta_a}{\sin\theta_w} = n \tag{1}$$

where n is a constant, which depends on the relative properties of the transmission media, the wavelength of the incoming electromagnetic radiation and temperature. For a 532-nm laser passing from air to water, $n = 1.33538$ (Damion and Masmura, 2007) and varies by less than 1% (±0.007) for a wide range of temperature and salinity conditions (Butler *et al*., 2002). Both θ_a and the co-ordinate of laser contact with the water surface x_w can be found from Figure 2 using simple trigonometry. From the apparent position of each underwater point (x and z), the real point location (x_r and z_r) can then be obtained as

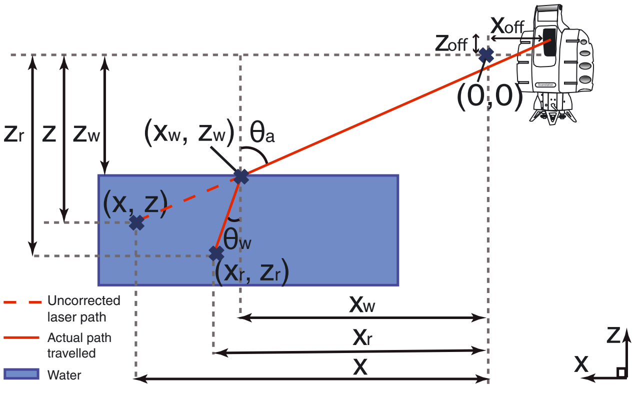

Figure 2. Geometry of the through-water terrestrial laser scanning refraction correction. Source: Smith *et al*. (2012, p. 412). This figure is available in colour online at wileyonlinelibrary.com/journal/rra

$$z_r = \frac{\cos\theta_w (x - x_w)}{n \sin\theta_a} + z_w \tag{2}$$

and

$$x_r = \frac{x - x_w}{n^2} + x_w \tag{3}$$

Because the geometry of refraction is unique for each point, the correction must be performed separately on each point in the through-water cloud.

Sensitivity analysis demonstrates that the refraction correction is most sensitive to the specification of the water surface level z_w in the local TLS survey co-ordinates. Where a relatively simple water surface can be assumed (a planar surface, for example), the vertical distance between the water surface and defined features observed in the point cloud can be surveyed in the field. Several such measurements are sufficient to fit a plane. Alternatively, a marked change in intensity of returns or defection of vertical markers placed in the water column can be used to estimate water surface height. In practice, intensity returns provide a reliable and distributed estimate of water surface height (described later). Where a more complex water surface is observed (e.g. pronounced surface waves and hydraulic jumps), specification of this parameter is problematic, and the angle of incidence must be adjusted to account for pronounced local water surface slopes.

Finally, the horizontal and vertical offsets are required to establish the actual angle of incidence of the laser at the point where it intercepts the water surface (x_w and z_w, respectively). This requires knowledge of the internal architecture of the specific TLS system. However, the magnitude of the horizontal and vertical offsets can be estimated through experiments with geometrically simple objects to model z_{off} and x_{off} inversely (Smith *et al*., 2012). z_{off} was estimated to be 0.012 m (±0.005 m) and $x_{off} = 0.017$ m (±0.016 m). Although the latter parameter is subject to considerable uncertainty, the through-water correction was not observed to be sensitive to these parameters, especially for reach-scale surveys (Smith *et al*., 2012).

The effect of refraction on the surveyed submerged points is comprised of two distinct components. Refraction at the water surface shifts the apparent point position (x, z) away from the scanner origin and increases the returned point elevation (Figure 2). However, the reduced velocity through the water column has the opposite effect on point elevation. Because the actual through-water distance is shorter than the uncorrected path computed by the TLS (Figure 2), the apparent point position is more distant from the scanner origin and of a lower elevation than the actual point position. Both components shift the apparent point away from the scanner origin; however, the elevation correction can be either positive or negative depending on the dominant component, determined by the angle of incidence and water depth.

Laboratory experiments

Laboratory experiments were conducted to examine the effect of the following: (i) flow velocity (LE1); (ii) wind speed at the water surface (i.e. water surface roughness; LE2); (iii) SSC (LE3); and (iv) water colour (LE4) on through-water TLS. Returned points were compared with dry reference scans acquired from the same TLS station before surface inundation. Under ideal water conditions on a gravel surface, Smith *et al.* (2012) found a complex pattern of errors relating to a combination of both horizontal and vertical offset errors. To provide greater clarity of the magnitude and source of any resulting errors, LEs were limited to beds of planar geometry made of smooth Perspex.

Laboratory experiment 1—flow velocity. Repeat TLS surveys were acquired in a recirculating flume (0.078 m wide and 1.5 m long) under a range of flows. The recirculation from the collecting tank to the header tank is driven by an electric pump with three settings, giving flow rates of 0.25, 0.41 and 0.62 L s^{-1}. The flume slope was also adjusted from horizontal to a 5% slope over 1% increments to increase the flow velocity. Observed flow velocities ranged from 0.05 m s^{-1} to a maximum of 0.61 m s^{-1}. The maximum water depth in the flume was 73.5 mm.

Three TLS surveys were undertaken at each combination of flow rate and slope angle at a range of 2.7 m from the centre of the flume and 1.4 m above the flume bed. The TLS was located at the bottom end of the flume. The resolution of each of these scans was set to 2 mm from a 5-m range to ensure that a minimum point resolution of 2 mm was acquired throughout the flume. Twenty sampling zones were analysed along the entire length of the flume. Each of these was 60 mm in diameter. Because of the increasing distance from the TLS, the number of survey points within the sampling zone decreases with distance up the flume (from 1.12 to 0.20 points per square millimetre in each horizontal flume dry reference scan). A planar water surface was estimated along the flume. However, supercritical flow was observed at the top of the flume at 4% and 5% slopes. Here, local depth measurements at each sampling zone were also used to adjust the water surface parameter of the refraction correction as they were poorly described by the estimated planar water surface.

Laboratory experiment 2—wind speed. During the flow velocity experiments, surface instability was observed at higher flow rates. To isolate this effect, wind shear at the water surface was simulated on a static water body. This caused substantial disturbance to the water surface. Applying the same sampling scheme described for the flow velocity tests, the flume bed was scanned under dry conditions, wet conditions and three surface wind velocity settings. A fan located at the base of the flume simulated wind conditions of up to 6.0 m s^{-1} at the flume outlet. A slope of 5.5% was applied to maximize the effect of the fan on the water surface. Water was impounded at the flume base to prevent flow. Wind velocity was measured using a Kestrel 3000 pocket weather meter (Nielsen-Kellerman Co, USA) with a micro-impeller and stated accuracy of ±3%. Wind velocity was observed to decrease with distance up the length of the flume, but this effect was not pronounced, and surface disturbance was considerable throughout the length of the flume.

Laboratory experiment 3—suspended sediment concentration. A 200-mm-deep water tank was used to create a static water body for suspended sediment experiments. A single sampling zone of 0.1-m diameter was used to evaluate through-water scans. This was surveyed three times at a range of 2.11 m from a height of 1.93 m above the surface to a stated resolution of 2 mm (at a 3-m range). In each dry reference scan, this resulted in a point density of 0.35 points per square millimetre (i.e., slightly higher than the 2-mm resolution). The tank was filled to a water depth of 200 mm, and TLS surveys were conducted in clear-water conditions. Several drops of a concentrated sediment solution (silt–clay fraction, $<63\,\mu$m) were then added and mixed through the tank, and through-water TLS surveys were repeated. The SSC was increased incrementally in this manner until the number of point returns within the sampling zone dropped below an arbitrary threshold of 33% of the original dry surface scan. The water level was then dropped by 10 mm and the TLS survey repeated. There was insufficient time for particles to settle out of the water column. When $>33\%$ of the dry surface scan points were recorded, further sediment was added to the tank, increasing the SSC. This procedure identified a threshold of point returns in terms of both SSC and water depth. Finally, at the highest concentration, the solution was left to settle for 12 h before the experiment was repeated. According to Stokes' law, the silt fraction would settle during this time, leaving only the clay fraction in suspension.

Water clarity is commonly measured using the Secchi depth: the depth at which a black-and-white disc is no longer visible to the naked eye. However, an inconsistent relationship between laser water penetration and the Secchi depth has been reported for bathymetric airborne lidar (Guenther *et al.*, 2000) because this method does not measure reflection and scatter (Hilldale and Raff, 2008) as would be detected by a nephelometer. In this study, the transmittance of the solution was measured using a PerkinElmer Lambda XLS spectrophotometer (PerkinElmer, Inc., Waltham, MA). The spectrophotometer compares the fraction of light at a given wavelength that passes through a solution with a reference value (distilled water). Using a wavelength of 500 nm, close to that of the TLS, the absorbance of a water sample was recorded to a stated precision of ±0.003 A or 1% of the reading (PerkinElmer, 2008).

The SSC was measured using a 500-mL water sample extracted from the tank and weighed and reweighed after the water had evaporated. Extracted samples were replaced with clear water in the water tank before the subsequent survey. This yielded an estimate of the SSC. Small measurement errors were significant at low concentrations. Absorbance and SSC were found to be linearly correlated ($r = 0.89$, $P < 0.0001$). Data are plotted in terms of absorbance; however, important thresholds are also reported in terms of SSC.

Laboratory experiment 4—water colour. The procedure followed for the SSC tests described earlier was repeated using a water-soluble substance, without the presence of silt–clay particles. Spectrophotometric absorbance provides a proxy for water colour (Grayson and Holden, 2012) and was measured as detailed earlier. Water colour was also observed visually.

Field experiments

Field experiments were conducted to establish the accuracy and precision of the method under field conditions where additional errors may be introduced (for example, because of the more uneven and fluctuating nature of the water surface and bed topography). Experiments were undertaken in the headwaters of the River Noguera Pallaresa, Catalan Pre-Pyrenees, close to the town of Esterri d'Àneu. The bed surface material in the experimental sites was highly variable in terms of size (from boulders to gravel) and shape (from well-rounded to platy-disc particles). Channel width was around 17 m. Two experiments (FE1 and FE2) were carried out downstream from a small pumping station that occasionally increases water discharge from around 1 up to 20 $\mathrm{m^3\,s^{-1}}$ during releases for power generation. A through-water survey was compared against a dry reference survey obtained during a lower river stage (FE1) to test the accuracy of the through-water correction under field conditions. Daily releases created the opportunity to survey a section of the exposed bed that was inundated during releases. Releases lasted for a few hours and did not disturb the survey section. A further experiment (FE2) tested the maximum limits imposed by flow depth and flow velocity. Finally, in a different section upstream of the pumping station where flow conditions were steady, a reach-scale through-water TLS scan was conducted to test the range limitations of the method (FE3). The water was clear; therefore, it is not expected that suspended sediment or water colour influenced the survey accuracy, precision or resolution.

Field experiment 1—field accuracy and precision test. Proper field validation of the through-water method requires a comparison with sub-aerial TLS surveys. A large granite boulder on the river bank was surveyed from the opposite bank at a range of 17 m. Three TLS scans were performed during both low-flow conditions when the boulder was exposed and high-flow conditions upon water release. The surveyed bank section was 2.2 m in length and 0.65 m in height, and no pools of water were held on this surface during the low-flow period. Under high-water conditions, the maximum water depth was approximately 0.34 m whereas surface flow velocity was approximately 1.03 $\mathrm{m\,s^{-1}}$. Across this short patch, a horizontal water surface was assumed for refraction correction, estimated using intensity returns in the unprocessed TLS point cloud.

Field experiment 2—velocity and depth limits. Logistical factors limited the range of flow depths and velocities that could be examined in the laboratory. Likewise, surfaces exposed before the water release were not the deepest patches of the river. Thus, a second field test compared a through-water corrected scan of a gravel patch (approximately 1 m by 1 m in area) during shallow and moderate flows with the through-water corrected scan of a deeper, faster flow upon water release. Because there is no reference dry scan for comparison, only point precision and density were assessed. Shallow flows had a maximum depth of ~0.6 m and a surface flow velocity of approximately 0.51 $\mathrm{m\,s^{-1}}$. The deeper flows had a maximum depth of ~0.9 m and a surface flow velocity of approximately 1.33 $\mathrm{m\,s^{-1}}$. This represented an especially deep patch of the river and was selected as an end member of conditions observed. Whereas a horizontal water surface was appropriate for the shallow-water condition, for the deep-water condition, a planar water surface elevation was reconstructed from observations of point intensity; a break in slope close to a large boulder was observed; thus, the estimated water surface was fit to observations using linear regression downstream and upstream of this break in water surface slope with $R^2 = 0.98$ and 0.15, respectively. The poor fit upstream of the boulder reflects the observed fluctuating water surface (±0.01 m).

Field experiment 3—range effects. The final field test demonstrates the potential of the through-water technique to obtain high-resolution bed morphology at the reach scale. It is anticipated that submerged point density will decrease with range at a faster rate than sub-aerial surveys.

DOI: 10.1002/rra

A reach of the river upstream from the dam release was surveyed from two TLS stations. Flow conditions were very similar to the low-flow conditions described in FE1. The water surface was fit using intensity returns; these were well described by a plane with $R^2 = 0.97$ (left bank scan, $n = 30$) and 0.99 (right bank scan, $n = 25$). The variation of point density with range was calculated for both exposed and submerged surfaces. Additionally, reach-scale maps of bed topography, water depth estimates and point density were created.

Evaluation criteria

Refraction-corrected point clouds were evaluated using three criteria: point accuracy, precision and density. Whereas Hodge *et al*. (2009) and Smith *et al*. (2012) detailed a patch-scale TLS protocol, using point filters to remove unreliable or non-surface points, the evaluation presented herein does not apply such point filters as only planar bed surfaces were examined in the laboratory and point filtering would obscure any loss of precision observed from changing water conditions, which is the main focus of this investigation.

Point accuracy was evaluated using the elevation difference between each through-water TLS point and its nearest neighbour (NN) in a reference point cloud obtained from the dry surface, before water was applied. A planar search radius was applied because a three-dimensional search algorithm would preferentially associate points of a similar elevation. The resulting NN error is calculated by subtracting the refraction-corrected through-water point elevation from the dry reference point elevation. Thus, a negative NN error indicates that the through-water point is lower than the dry reference point. For FE1, where the surface under investigation is vertical, *y*-co-ordinates of points were compared. In this case, a three-dimensional search algorithm was implemented for NN analysis because the complex nature of the scans close to the riverbed caused mismatching of points when a planar search radius was applied.

Three repeat TLS surveys of each surface condition were conducted to evaluate the point precision. Precision was quantified using the repeat scan error value (RSEV), following Hodge *et al*. (2009). RSEV is defined as the maximum three-dimensional distance between repeat measurements of the same point, given by

$$RSEV = \max\left[\sqrt{\left(x_i - x_j\right)^2 + \left(y_i - y_j\right)^2 + \left(z_i - z_j\right)^2}\right] \quad (4)$$

where $x_{i\text{–}j}$, $y_{i\text{–}j}$ and $z_{i\text{–}j}$ are the co-ordinates of the point in scans *i* and *j*. Points in each scan on the same ray angle were identified. The term in square brackets is calculated for all possible pairs of scans (with three repeat scans, there are three possible scan pairs).

Finally, the density of returned points was expressed as a percentage of returns in the dry reference scan. An arbitrary threshold of 33% of original point returns was established as an acceptability criterion for this metric in laboratory tests. Given the initial dry scan point resolution of laboratory tests, this equates to approximately 5 points per square millimetre which should be sufficient for most patch-scale applications.

RESULTS

As a reference standard, Smith *et al*. (2012) reported NN error values of <5 mm for through-water scans obtained through a 200-mm depth of static, clear water on natural gravel surfaces. Moreover, there was no reduction in point returns or precision in comparison with dry reference scans.

Laboratory experiments

Laboratory experiment 1—flow velocity. The angle of incidence and water depth in this experiment were such that refraction shifts the apparent position of uncorrected TLS point returns to a higher elevation and more distant from the TLS origin. Refraction correction acts to lower points in this geometrical arrangement. Figure 3 presents NN errors for the three flow rates (Q1–Q3) at a selection of slope angles. Intermediate slope angles are not presented, for clarity. Table 2 summarizes the through-water evaluation in terms of flow velocity, classifying all sampling zones into 0.1-m s^{-1} flow intervals. A maximum flow velocity of $0.61\ \text{m s}^{-1}$ was observed in these experiments.

Nearest-neighbour errors are mostly <5 mm, and corrected points are lower than the dry reference clouds. In sub-critical flow conditions, absolute NN errors are similar in magnitude to those observed at comparable water depths under static, clear-water conditions (a mean NN error of 2.32 mm at 100-mm depth is reported by Smith *et al*., 2012). Point precision (RSEV) and density values are encouraging in each experiment and show no pattern along the flume length. Point precision is unaffected by flow velocity and Froude number; point density does drop where $\text{Fr} > 1$, although these values remain acceptable (>50%).

Figure 3a–c shows that at low slope angles, NN error does not increase with increasing flow rates. Over-lowering increases slightly with distance up the flume. This may result from either the increasingly oblique scanning angle or the increase in flow velocity observed towards the top of the flume; however, as flow rate increase has little effect at lower slope angles, the scanning angle effect is the more likely explanation.

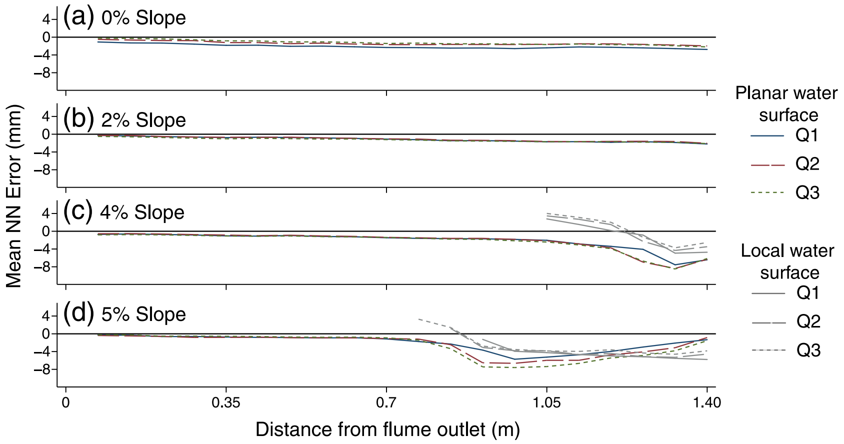

Figure 3. The effect of flow velocity on point accuracy (LE 1): (a–d) variation of mean nearest-neighbour (NN) error along the flume at different slopes and flow rates (grey lines represent repeat through-water corrections using local water surface elevation measurements, shown only where flow was supercritical; see text for details). Q1, Q2 and Q3 represent flow rates of 0.25, 0.41 and 0.62 L s^{-1}, respectively

At flume slopes of 4% and 5%, supercritical flow is observed at the top of the flume. This gradually propagates down the length of the flume with increasing slope and flow rate with a noticeable effect on NN error (Figure 3c, d). Figure 4 shows that NN errors are clearly related to the Froude number and increase markedly where Fr > 1 (also Table 2). Naturally, where supercritical flow is observed, a planar water surface is wrongly specified, and the actual flow depth is less than estimated. The refraction correction is too severe because in reality the laser propagates through only a shallow-water column. Repeat through-water corrections with measured local water surface elevations reduce this error (grey lines, Figure 3c, d). However, the increase in NN error and in the variability of errors in the supercritical regime remains apparent. This is especially significant given the typically low-flow depths observed at these points (~10 mm).

Laboratory experiment 2—wind speed. To isolate the effect of water surface instability, surface wind speeds up to 6.0 m s^{-1} created an uneven, fluctuating water surface on an otherwise stationary water body in the flume. Table 3 summarizes the point accuracy, precision and density at each of three wind velocity settings. The distribution of mean NN errors (across all sampling zones) observed within the flume is displayed in Figure 5. Again, refraction correction lowered the uncorrected through-water point cloud and brought each point closer to the TLS origin. NN errors show that corrected points are lower than those in the dry surface reference scan. These errors range between −0.3 and −4.5 mm. Because the flume slopes towards the scanner origin, refraction correction is either lowering points excessively or shifting points insufficiently towards the TLS origin. The negative NN errors observed for a horizontal flume (LE1) suggest that over-lowering is the more likely component.

Although mean NN errors increased slightly with increasing wind velocity (Figure 5 a), these remain within acceptable levels and are similar in magnitude to those observed under ideal conditions (<5 mm). An increase in mean NN error of

Table II. The effect of flow velocity on point accuracy, precision and density

Flow velocity range (m s^{-1})	Number of sampling zones	Mean Froude number	Mean nearest-neighbour error (mm)	Mean repeat scan error value (mm)	Mean % returned points
0–0.1	152	0.01	−1.12	6.61	85.42
0.1–0.2	144	0.19	−1.22	5.49	80.45
0.2–0.3	16	0.54	−1.83	5.04	86.42
0.3–0.4	17	1.01	−3.73	5.25	69.31
0.4–0.5	17	1.36	−4.61	5.82	60.54
0.5–0.61	14	1.58	−5.18	6.28	54.84

All measurements are classified into intervals of 0.1 m s^{-1} for clarity. Because of changing slopes, a range of velocities was observed at each discharge setting. The final bin is slightly expanded to encompass the full range of measurements. Results are for planar water surface corrections only.

DOI: 10.1002/rra

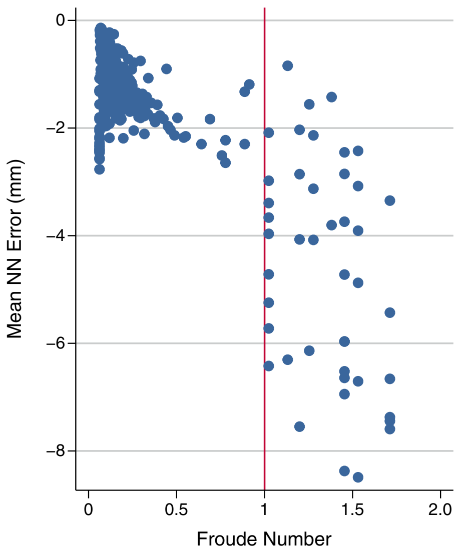

Figure 4. The effect of the Froude number on point accuracy (nearest-neighbour, NN, error) where a planar water surface is assumed (LE 1). This figure is available in colour online at wileyonlinelibrary.com/journal/rra

a similar magnitude is observed with increased flow velocity where flow remains sub-critical (Table 2). At each setting, the difference between the NN error and that observed with no surface wind is largest at the bottom of the flume and decreases with distance from the wind source. Point precision decreased with increasing wind velocity (i.e. RSEV increased; Figure 5b), but this effect was also relatively minor given that there was considerable water surface disturbance observed. Point density remained unaffected by surface instability with >95% of dry reference points returned at each wind setting.

Laboratory experiment 3—suspended sediment concentration. The density of bottom returns was affected by both water depth and SSC. Figure 6 plots each through-water test conducted on the basis of water depth and measured absorbance at 500 nm. Experiments were classified according to the point density acceptability criterion (>33% of dry scan points) and were conducted in order, moving from bottom-right to top-left of the graph space. The final acceptable scan at each water depth is displayed as a dark ring. As water depth was decreased, the absorbance level (or SSC) at which an acceptable number of point returns was achieved increases. To obtain a minimum estimate of the absorbance threshold at each water depth, the final pass at each depth was taken as the threshold value, although in reality, the threshold will be constrained by this final acceptable survey and the failed survey (indicated by a cross). The regression line in Figure 6 demonstrates that a strong linear relationship between SSC and flow depth was observed ($R^2 = 0.952$, $n = 10$). The point density threshold is underestimated at high values of SSC, but the close fit suggests that a linear model is appropriate within this range.

Figure 6 also displays the distribution of NN errors for selected experiments (a–m). Values of the mean NN error and RSEV are also displayed. For comparison, Figure 6a displays the distribution of NN errors for the clear-water condition (at 200-mm depth). After the silt fraction of the highest SSC level (l) had been left to settle (m), the calculated NN errors returned to the clear-water value. For this experiment, absorbance was also low, suggesting that silt particle sizes had the largest effect on the through-water surveys.

Despite the low number of point returns above the identified linear threshold, mean NN error was <5 mm in experiments indicated by inset graphs in (e) and (c). These point accuracy values are comparable with the clear-water reference condition (a) and survey through-water conditions below the point density threshold (f and d). A similar effect can be seen for point precision; with the exclusion of (e), RSEV is <9 mm for these experiments. Thus, point accuracy and precision appear unrelated to water depth and are influenced by a separate threshold of SSC alone. This second threshold is indicated in Figure 6 as a horizontal line and corresponds to an SSC of approximately 0.11 g L^{-1}. The tank images display the water surface at SSC levels immediately above and below this threshold. Where water was below the sloping point return threshold

Table III. The effect of surface wind velocity on point accuracy (nearest-neighbour, NN, error), precision (repeat scan error value, RSEV) and density (percentage of returned points) over the flume

Surface wind velocity (m s^{-1})	Mean NN error (mm)		Mean RSEV (mm)		Percentage of returned points	
	Mean	Minimum	Mean	Maximum	Mean	Minimum
(Dry) 0.0	—	—	4.99	4.99	100.00	100.00
(Wet) 0.0	−1.75	−4.01	5.06	5.06	97.00	94.10
2.7	−1.78	−4.32	5.19	5.19	97.31	93.32
5.3	−2.00	−4.36	5.38	5.38	96.95	93.41
6.0	−2.40	−4.54	5.53	5.53	97.01	92.79

Mean NN error and RSEV for each sampling zone are presented. For each metric, values for the flume mean and the worst-performing sampling zone are given.

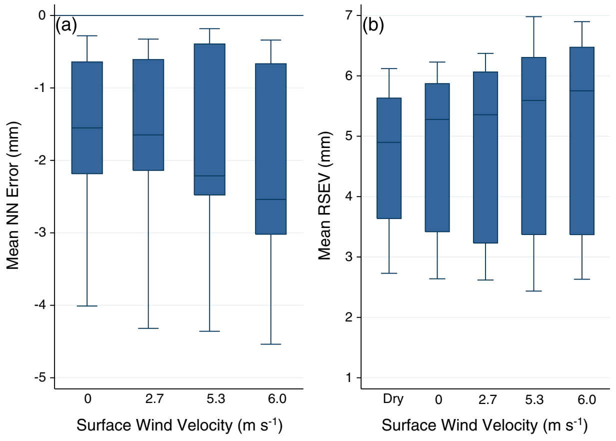

Figure 5. Distribution of (a) nearest-neighbour (NN) errors (in mm; representing accuracy) and (b) repeat scan error values (RSEV, mm; precision) at each wind velocity setting (LE 2). Boxes show upper quartiles, medians and lower quartiles; whiskers extend to cover all points. This figure is available in colour online at wileyonlinelibrary.com/journal/rra

yet above the SSC threshold (h), low point accuracy and precision was observed. Surveys in water conditions above both thresholds (j, k and l) performed poorly on all metrics, and non-bed points are clearly returned. Scans in conditions close to the thresholds (g, i and h) show two separate populations of point returns, the lower of which approximates the bed elevation.

The horizontal SSC threshold line in Figure 6 has a significant effect on point accuracy and precision. Figure 7a,b plots each experiment as a residual from this threshold line and demonstrates a clear effect on NN error and RSEV. Points above the 0.11-g L^{-1} threshold are plotted to the right of the vertical line. Mean values are plotted as symbols; range bars represent ±1 standard deviation. Because the standard deviation of accuracy and precision values above and below the threshold were unequal, Wilcoxon rank-sum (Mann–Whitney) tests were applied to test for significant differences above and below this threshold. In both cases, significant differences were observed with $P < 0.0001$. Significant but much weaker differences were also observed using the point return threshold (regression line in Figure 6; data not presented). The outlier on the left of Figure 7b has a lower precision than expected; however, this point is plotted above the point density threshold and contains comparatively few data points.

Laboratory experiment 4—water colour. A similar relationship between absorbance at 500 nm and water depth is observed for soluble components of light attenuation alone (Figure 8). As absorbance by soluble components increases, the depth at which the laser could achieve a sufficient number of bottom returns decreases. In these experiments, the threshold was much more defined; point clouds contained either close to 100% of the number of points in the dry surface reference scan or a very low number of points (if any at all). As in the SSC experiments earlier, a defined threshold line for point density can be observed in terms of absorbance and water depth. Again, a strong fit was observed; however, with the presence of only dissolved material and no particulate component, the absorbance threshold was an inverse function of water depth ($R^2 = 0.987$, $n = 11$).

Inset graphs show the distribution of NN errors for selected experiments (Figure 8a–g; note the different y-axis scales from the inset graphs of Figure 6). The error distribution observed under a reference condition of a clear-water column of 200-mm depth is presented in Figure 8a. Point accuracy is unaffected by the presence of dissolved particles. All through-water scans have a mean NN error of <5 mm, similar to clear-water conditions. Figure 7c shows that the point density threshold has no effect on point accuracy; a Wilcoxon rank-sum test confirms that no significant difference in point accuracy can be detected either side of the inverse point density threshold. Thus, although few points were returned above this threshold, they were an accurate representation of the underlying surface. Conversely, point precision follows the same threshold identified for point density (Figure 7d). The significance of this is confirmed by a Wilcoxon rank-sum test ($P < 0.005$). It should be noted, however, that RSEV values above the point density threshold are based on very few returned points and may simply be an artefact of the low point density.

Field experiments

Field experiment 1—field accuracy and precision test. Images of the surveyed gravel boulder at high and low flows are shown in Figure 9 alongside the photo-rendered point cloud during low-flow conditions. Figure 9d displays points from a 50-mm-wide transect from the centre of the study region of dry and uncorrected through-water points alongside refraction-corrected points. Refraction has shifted the submerged uncorrected points to be higher and more distant from the point of origin. Refraction correction successfully adjusts for this large difference; however, a discrepancy remains, and most corrected points have been shifted closer to the point of origin than necessary, resulting in negative NN values. Figure 9e shows the distribution of NN errors in the corrected point cloud for submerged points only. The median NN error is −7.06 mm with a standard deviation of 1.20 mm. Several outliers are observed in this distribution. The depth dependency of this value is shown in Figure 9f, calculated in elevation bands of 50 mm. The rapid increase beneath the water surface is apparent and, aside from a reduction at 0.3-m

DOI: 10.1002/rra

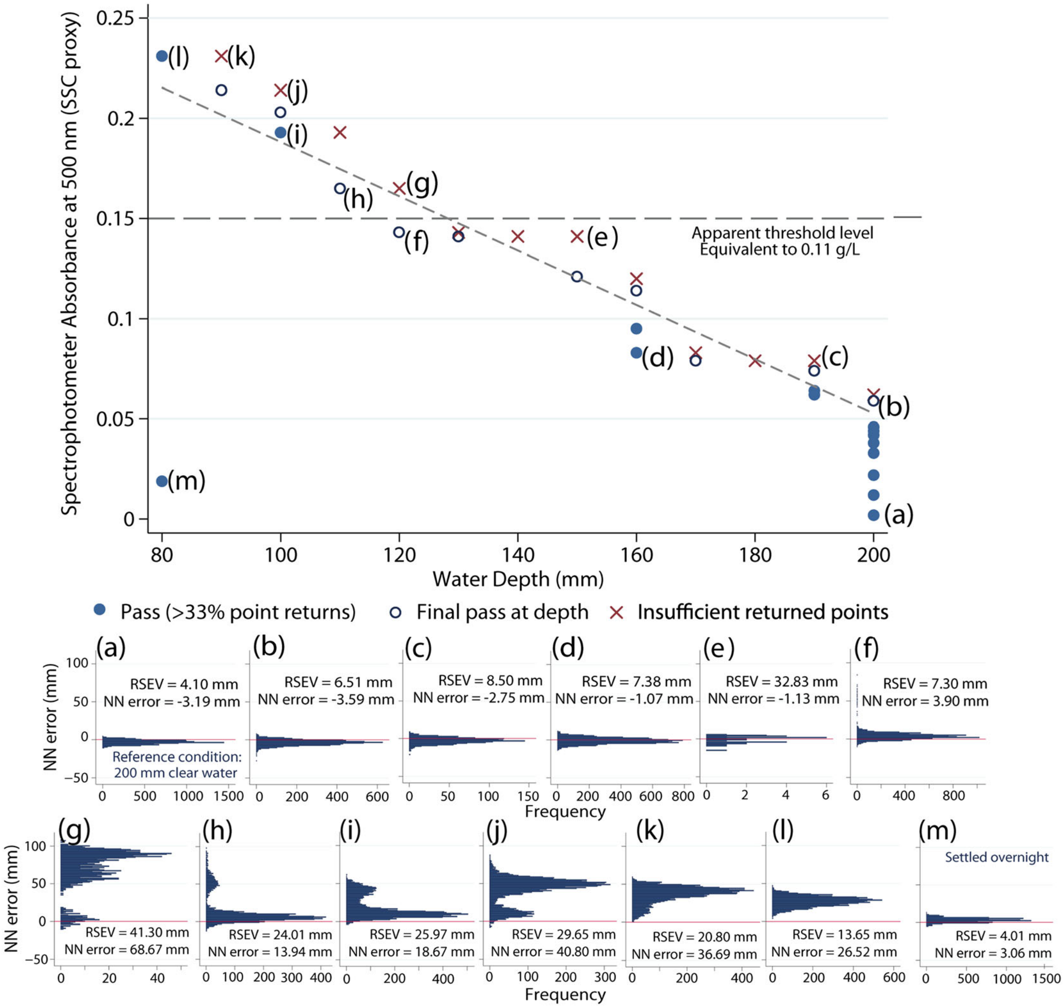

Figure 6. The effect of water depth and suspended sediment concentration (SSC, or absorbance) on the percentage of point returns (LE 3). A linear relationship between absorbance and depth is observed at the threshold for acceptable point density (absorbency = −0.0014 * depth + 0.32). Distributions of nearest-neighbour (NN) error at selected sediment and depth conditions are also presented (inset graphs). These are generally acceptable below an SSC threshold of 0.11 g L^{-1} (top row, a–f). RSEV, repeat scan error value. This figure is available in colour online at wileyonlinelibrary.com/journal/rra

water depth, remains relatively constant for deeper points. NN errors are an order of magnitude greater than those seen above the water surface. Median RSEV values are also an order of magnitude greater than those for the exposed surfaces at 20.08 and 2.01 mm (with respective standard deviations of 25.86 and 1.62 mm). Figure 9g shows that this value increases steadily with depth; however, the large increase towards the base of the bank may be due to the three-dimensional nature of the surface where mixed pixels (multiple returns for a single laser pulse) inflate RSEV (Hodge *et al*., 2009). These low-precision points occur when scanning all surfaces of complex geometry and would normally be filtered before further analysis.

Field experiment 2—velocity and depth limits. For clarity, Figure 10 shows a 20-mm-wide transect through the point clouds obtained for a 1-m^2 patch. Estimated water surface elevations for both deep and shallow surveys are also indicated. The shallow-water scan displays dense bottom returns throughout the submerged portion of the patch (0.44 points per square millimetre compared with 0.47 points per square millimetre over the exposed area of boulder). Despite being obtained through deeper water than the previous test, the median RSEV value for the submerged points is much lower at 6.02 mm. This is most likely a consequence of the less-oblique angle of incidence and consequent reduction in the number of mixed pixels. In deeper, faster flows, several water surface points are observed, the upper of which match the estimated water surface closely. Similar surface points were observed using a near-infrared TLS by Milan *et al*. (2010). In addition, bed points are observed on the large boulder on the

DOI: 10.1002/rra

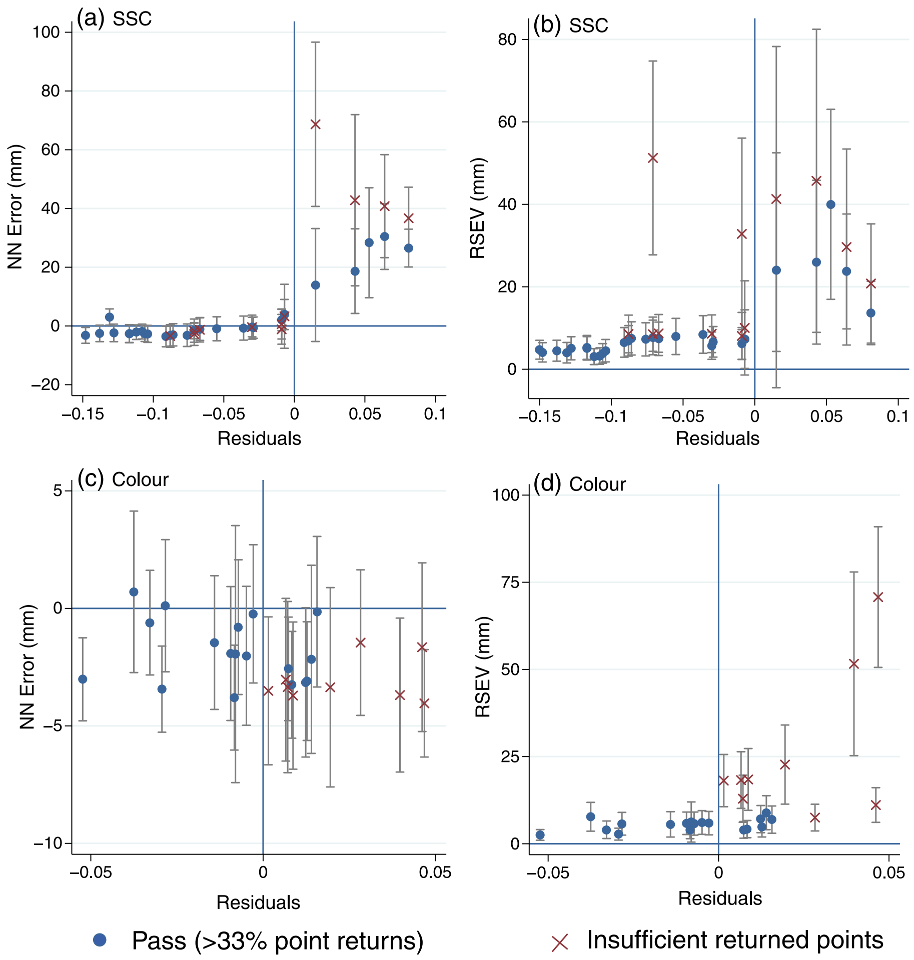

Figure 7. The effect of identified thresholds on point accuracy (nearest-neighbour, NN, error) and precision (repeat scan error value, RSEV) for suspended sediment concentration (SSC, 0.11 g L^{-1}; horizontal line in Figure 5) (a, b) and water colour (inverse relationship; Figure 8) (c, d). Residuals represent the deviation of each point from threshold lines (positive values represent points above the thresholds in Figures 6 and 8). Symbols are plotted at mean values and represent point density criterion pass (circles) or fail (crosses). Grey lines represent ±1σ. This figure is available in colour online at wileyonlinelibrary.com/journal/rra

downstream edge of the profile. A threshold water depth of 0.68 m can be identified beyond which no bed points are returned. This threshold depth will be reduced for particularly oblique surveys. Where both surface and bed points are returned, water surface points represent just 3.77% of total returned points. With the exclusion of these water surface returns, median RSEV is 13.47 mm. NN errors were calculated where the boulder was exposed during shallow flows; the median value of −7.73 mm is similar to the value observed in the previous test.

Field experiment 3—range effects. A reach of the river upstream from the pumping station was surveyed from two TLS stations (Figure 11a) during average flow conditions (i.e. 1 m^3 s^{-1}). Water depths up to 0.5 m were observed under such conditions. Average water depth was around 0.1 m ($\sigma = 0.08$ m). The reach was scanned from two stations and registered using four reflective round targets. The three-dimensional registration error was 9 mm. A map of point densities for the entire reach is presented in Figure 11a. To avoid possible interferences caused by the registration process, the resolution of point clouds from just one TLS station (station 1) was investigated. Results are presented in Figure 11b, c.

The water surface was fitted using intensity returns across the reach as described in the Methods section. The highest resolutions (i.e. >5 points per square centimetre) are observed near the TLS (0–10 m; once the range increases to >10 m, the resolution decreases (<1 point per square centimetre). This effect is also observed in sub-aerial surveys. Overall, Figure 11b demonstrates that, with a carefully planned survey strategy, high-resolution surveys of submerged topography can be achieved.

The point cloud was spatially filtered using TOPCAT software (Brasington *et al.*, 2012; Rychkov *et al.*, 2012) to

DOI: 10.1002/rra

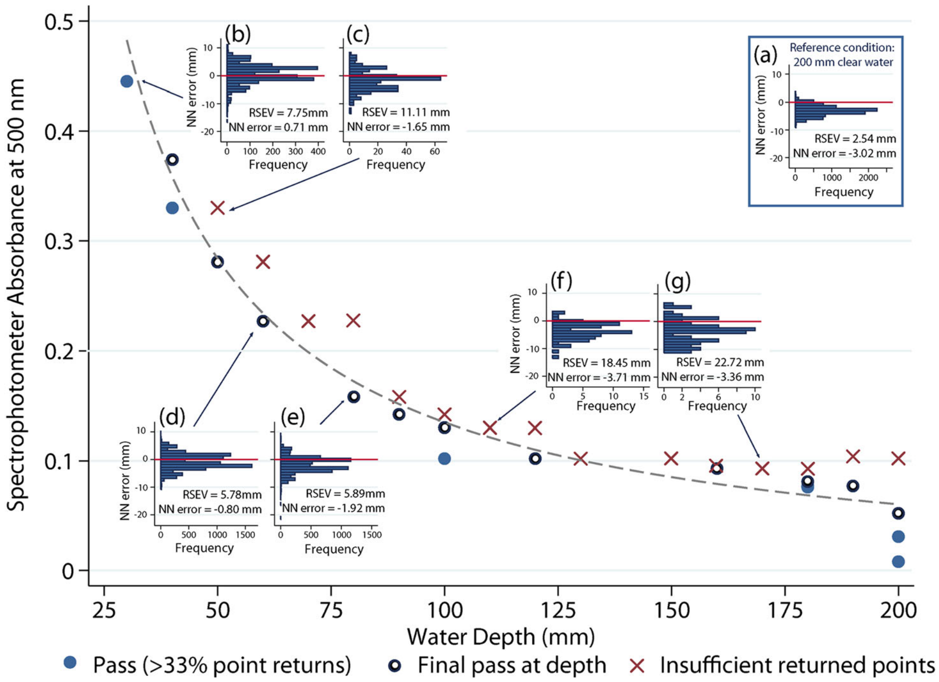

Figure 8. The effect of water depth and colour (absorbance) on the percentage of point returns (LE 4). An inverse relationship between colour and depth is observed at the threshold for acceptable point density (absorbency = 14.90 * (depth)$^{-1}$ – 0.01). Distributions of nearest-neighbour (NN) error at selected absorbance and depth conditions are also presented (inset graphs). RSEV, repeat scan error value. This figure is available in colour online at wileyonlinelibrary.com/journal/rra

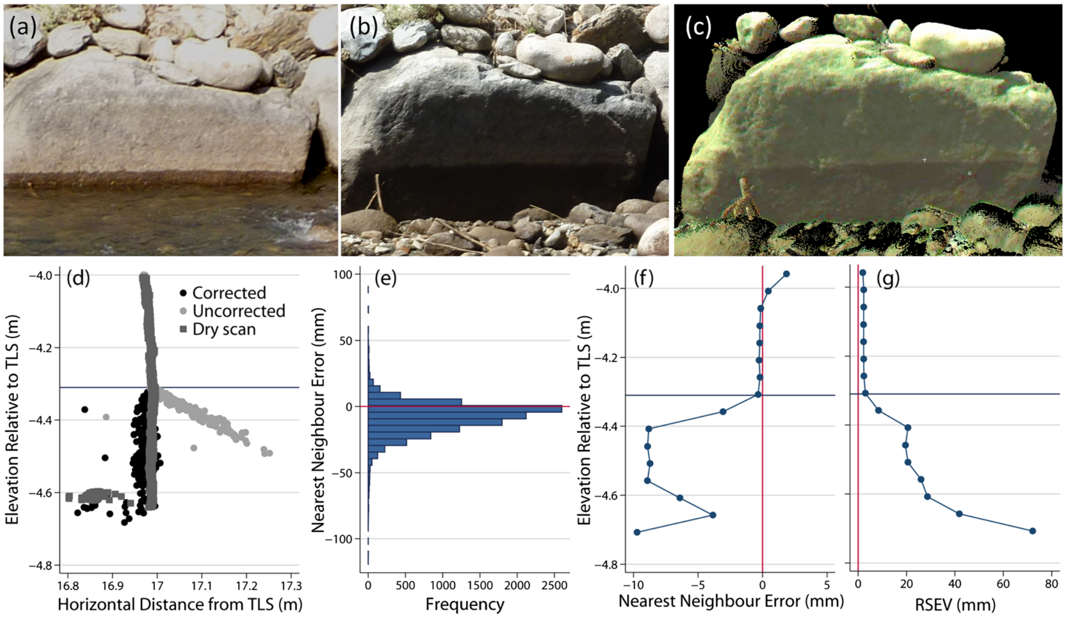

Figure 9. Field experiment to determine point accuracy and precision of boulder bank survey (field experiment 1): (a) deep-flow and (b) shallow-flow conditions; (c) point cloud from shallow-flow conditions; (d) sample of points within a 50-mm-wide transect through the centre of the surface (terrestrial laser scanner positioned to the left); (e) nearest-neighbour (NN) errors of the submerged, corrected points; (f) variation of NN error and (g) repeat scan error value (RSEV) with depth. Horizontal lines indicate estimated water surface elevation. This figure is available in colour online at wileyonlinelibrary.com/journal/rra

DOI: 10.1002/rra

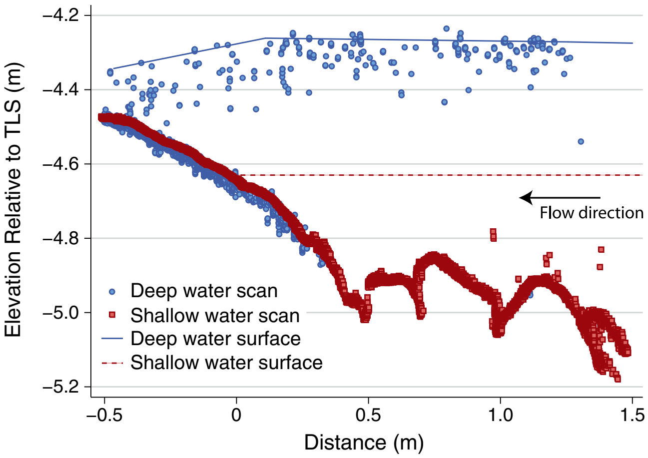

Figure 10. Comparison of shallow-water and deep-water refraction-corrected point clouds from a 20-mm-wide transect through the centre of the patch (FE 2). Estimated water surfaces are indicated. This figure is available in colour online at wileyonlinelibrary.com/journal/rra

extract local statistics at a horizontal grid resolution of 1 m. The minimum elevation in each grid was then used to elaborate the flow depth map presented in Figure 11c. Large bed structures such as boulders can be identified easily, alongside pools and shallow riffles. To study the limits of our approach, we subsequently selected a 10-by-10-m section. Raw data within this section were filtered using TOPCAT but at a 0.05-m grid resolution. Results are presented in Figures 11d (density) and e (flow depth). Coarse gravels can be identified from the data, and water depth between big boulders can be mapped at the reach scale.

Figure 12a demonstrates the effect of range on point density for sub-aerial and submerged field data separately for a cross-channel profile (indicated on Figure 11c). Density decreases with distance for both sub-aerial and submerged points with no real difference between the two. Beyond 11 m, the opposite bank is reached, and no further submerged points are found. To further examine the effect of range on through-water surveys, adjacent patches were compared (one sub-aerial and one submerged) at two locations: close to the scanner origin (~4-m range; 0.12 m^2) and far from the origin (~11 m; 0.7 m^2) (Figure 12b). Patch size increased with range to provide an equal number of point returns for analysis. Frequency densities of point density are plotted for each patch. Mean point densities are comparable for both above-water and submerged patches, although point density does drop off more rapidly with distance for the submerged patches.

DISCUSSION

This paper has examined the effect of flow velocity, surface wind shear, SSC and water colour on the accuracy, precision and density of through-water TLS. Over 300 scans performed in laboratory experiments were supplemented with three field tests of the method to investigate the range of water conditions (in terms of both hydraulics and suspended sediment transport) for which through-water TLS can acquire high-resolution fully three-dimensional representations of gravel beds in fluvial settings. The main findings are summarized in Table 4. It should be noted, however, that combined effects of each of the variables examined have yet to be tested. Many more experiments would be required to produce a full error budget for the variables investigated; however, for future field applications, Table 4 does provide sufficient information to estimate error arising from through-water scanning.

Stated errors are additional to those observed in sub-aerial TLS surveys and investigated thoroughly by Hodge *et al.* (2009). Point accuracy and precision values in some laboratory conditions were superior to those reported under ‘ideal conditions’ by Smith *et al.* (2012). This improved bed representation can be explained by the planar bed surveyed here. The largest vertical errors reported by Smith *et al.* (2012) were partially due to sharp surfaces located at the edge of gravel clasts, where a large vertical error arises from a small horizontal error. Conversely, the smooth sloping surfaces used in laboratory tests prevented this effect from dominating the reported errors, although they would remain detectable.

Results emphasize the importance of specifying the water surface elevation correctly before refraction correction. A simple planar water surface was insufficient where supercritical conditions were present and the water depth was overestimated. Steeply sloping water surfaces as observed at hydraulic jumps and drops will also influence the angle of incidence and alter the degree of refraction. A range of rough water surfaces has been observed on rivers by Milan *et al.* (2010). Out-of-plane refractions must also be accounted for when surveying from a direction perpendicular to any steep water surface slope. Specifying water surface height on the basis

DOI: 10.1002/rra

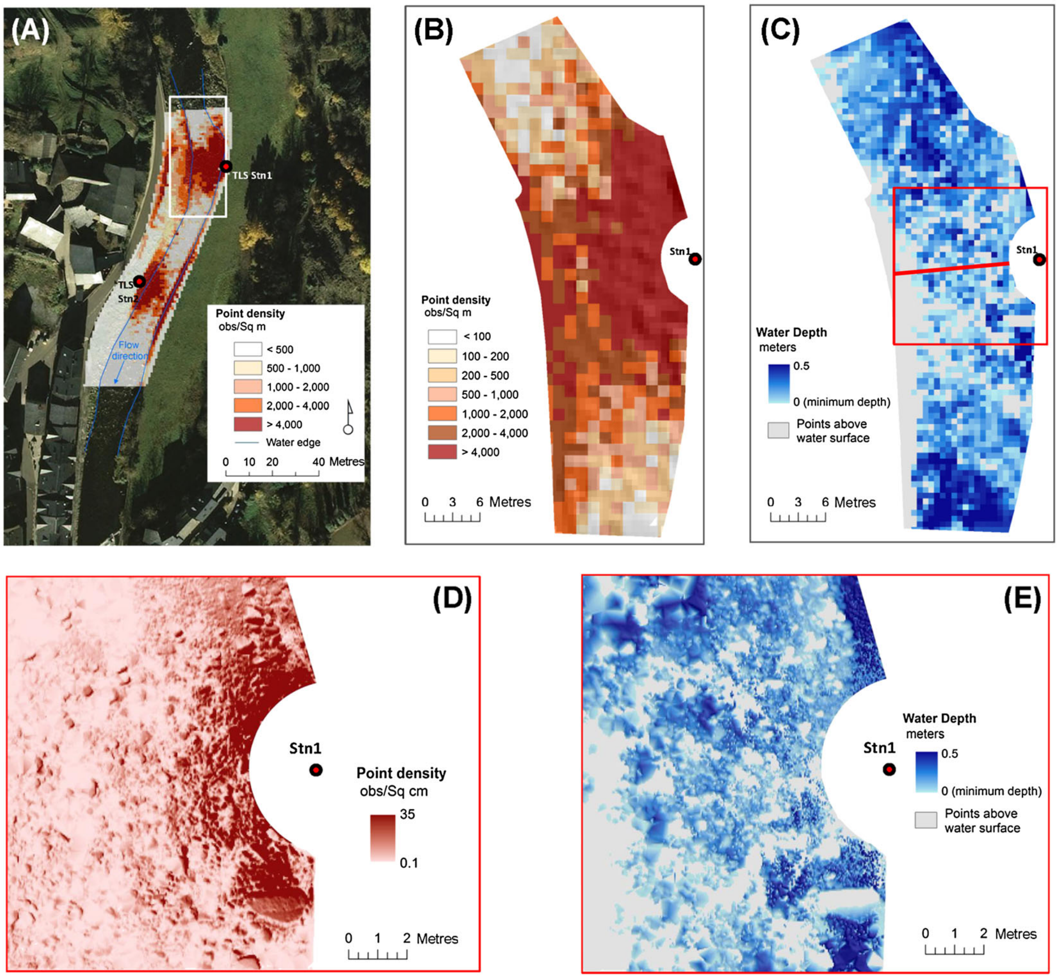

Figure 11. Reach-scale through-water topography of the Noguera Pallaresa. (A) Map of point density (m^{-2}) for the whole reach mapped at 1-m resolution; (B) point density (m^{-2}) and (C) estimated depth (m) from a single terrestrial laser scanning station mapped at 1-m resolution; (D) density and (E) depth mapped at a 0.05-m resolution. This figure is available in colour online at wileyonlinelibrary.com/journal/rra

of local measurements and observed changes in intensity improves accuracy. At the reach scale, water surface elevation estimates can be improved further by interpolating a larger number of edge points (Brasington *et al*., 2003; Westaway *et al*., 2003). In the laboratory wind speed tests, a disturbed water surface yielded only a minor decline in point precision (Figure 5). In field situations, where potentially large and fluctuating water surface irregularities cannot be mapped accurately, the accuracy and precision of through-water TLS will decrease markedly. However, in most situations where irregularities are small (as observed in laboratory wind speed experiments), the method remains appropriate. A field test demonstrated that although additional errors were observed, they remained <10 mm. Although surveys across an entire river reach are possible, gaps do exist, in white-water conditions, for example. Carbonneau *et al*. (2006) also reported that such areas are unsuitable for optical–empirical reflectance depth mapping.

As the laser pulse is attenuated exponentially with water depth (Lyzenga, 1981; Wang and Philpot, 2007), in clear-water conditions with gravel beds, through-water TLS using the Leica ScanStation C10 has a maximum depth penetration of around 0.68 m. It is likely that many green-wavelength TLS devices will demonstrate similar depth limits, although this will be dependent on the geometry of the individual survey. Although this is relatively shallow, it is sufficient for many mountain and braided stream reaches in low-flow conditions. Winterbottom and Gilvear (1997) reported a similar upper depth limit of 0.6 m for the optical–empirical reflectance depth technique, although Westaway *et al*. (2003) observed a higher limit of 1 m. Power limitations for eye safety means that the greater water penetration of airborne bathymetric lidar (<60 m) is achieved by increasing the laser footprint size, thereby decreasing sample resolution. Through-water TLS surveys are not as extensive as these aerial remote-sensing methods; however, the resulting data

DOI: 10.1002/rra

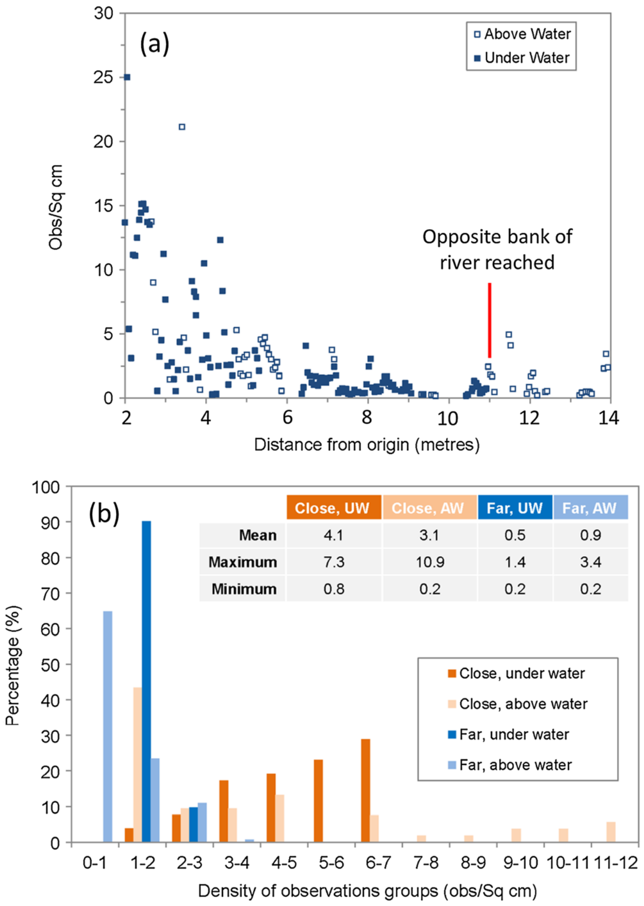

Figure 12. The effect of range on point density for sub-aerial and submerged topography. (a) Point density with distance from the terrestrial laser scanning (TLS) origin for above-water (AW) and underwater (UW) cells for a profile in Figure 11c; (b) frequency density of point density calculated for four patches (UW and AW patches both close to and far from the TLS origin). Summary data are shown in the inset table. This figure is available in colour online at wileyonlinelibrary.com/journal/rra

are of a higher resolution and form part of a single integrated sub-aerial and submerged TLS survey, which requires little additional financial resource to implement, providing near-particle-scale topographic models to study channel morphodynamics, hydraulics and their interaction with riverine habitat conditions.

At high flow velocities (>1 m s^{-1}), a number of near-surface returns were observed in the field, although these had a negligible effect on bed point density. However, where laser absorbance and scattering of the water column was increased by particulates and solutes, the density of point returns was the limiting factor at much shallower depths. Nevertheless, images of the water column in Figures 6 and 8 show that through-water TLS is possible through shallow, turbid and dark water columns even where the bed is not visible. Where the particulate component was dominant, scattering and absorption by silt particle sizes in the water column gradually reduced the number of point returns. Laser attenuation is related to both the SSC and the distance the laser travels through the water column. The threshold relationship was linear; however, where only soluble components were present, a more defined inverse relationship was observed. A comparison of the threshold regression lines (Figures 6 and 8) suggests that the two thresholds may be similar. Because no accurate bed survey points were observed at high SSC levels, experiments were terminated at a minimum depth of 80 mm, whereas water colour experiments continued to a minimum depth of 30 mm. The water colour threshold approximates a linear relationship over the same range as the SSC experiments ($R^2 = 0.924$, $n = 7$); the possibility that the thresholds are the same (i.e. both possibly inverse in nature) is further supported by the observation of slight underestimation by the regression line at lower depths for the SSC threshold (Figure 6). Extrapolation of these thresholds to deeper flows must be treated with caution and requires further investigation.

With particulates in the water column, through-water TLS is limited by point accuracy and precision at concentrations of >0.11 g L^{-1}. This concentration is far above the minimum concentration (or even average SSCs) obtained in

DOI: 10.1002/rra

Table IV. Summary of the limiting conditions on through-water terrestrial laser scanning

	Point accuracy (nearest-neighbour error)	Point precision (repeat scan error value)	Point density (% of dry scan points)
Flow velocity (Figures 3 and 4; Table 2)	**Acceptable (i.e. <5 mm) where flow is sub-critical. Minor effect of surface instability (<10 mm)**	No substantial effect (<7 mm) observed up to cross-sectional average velocities of 0.61 $\mathrm{m\,s^{-1}}$	Acceptable (i.e. $>33\%$) across range of flows. Minor drop where supercritical. Small number of surface points in high flows
Flow depth (clear water; Figures 9 and 10)	No depth dependency of error observed beyond the initial increase	No conclusive depth dependency, although slight decreases with depth observed	**No returns observed below 0.68-m depth**
Surface wind speed (Figure 5; Table 3)	Acceptable to at least 6.0 $\mathrm{m\,s^{-1}}$: only very minor effect of surface instability observed	Acceptable (i.e. <10 mm) to at least 6.0 $\mathrm{m\,s^{-1}}$: only very minor effect of surface instability observed	Unaffected to at least 6.0 $\mathrm{m\,s^{-1}}$
Suspended sediment (particulate component; Figures 6 and 7)	**Limited by a 0.11-g $\mathrm{L^{-1}}$ threshold. Independent of water depth**	**Limited by a 0.11-g $\mathrm{L^{-1}}$ threshold**. More data required to confirm independence of the depth-dependent density threshold	**Linear limiting threshold between depth and suspended sediment concentration; apparent when depth >120 mm**
Water colour (soluble component; Figures 7 and 8)	Unaffected	Possible effect of inverse threshold identified for point density. More data required	**Defined inverse limiting threshold between depth and absorption**
Angle of incidence/range (Figures 9, 11 and 12)	No additional error observed at longer ranges	**Decrease in point precision at longer ranges (20 mm at 17-m range)**	**High-resolution surveys at ranges <15 m. Slightly more rapid decrease with range**

Limiting factors are highlighted in bold.

DOI: 10.1002/rra

cobble–gravel shallow beds. For instance, in the mountainous Ribera Salada catchment in the Southern Pyrenees, the mean SSC during three consecutive hydrological years is estimated at around 15 mg L^{-1} (Vericat and Batalla, 2010). Values close to the threshold were sampled during low-magnitude flood events, and although concentrations up to 3 g L^{-1} could be obtained during flood events, during such conditions, water surface roughness and depth could be additional limitations. At high SSC levels, returned points within the water column obscure the bed; this is clearly demonstrated where two separate populations of points at different elevations are observed. Further experiments at depth and SSC values close to the two thresholds in Figure 6 are required to confirm which threshold determines point precision. Backscattering in the water column may also produce mixed pixels and explain the decrease in point precision observed at large ranges in the field (Gao, 2009).

Through-water TLS at the patch scale can be conducted to a high accuracy, precision and resolution under a range of flow conditions. Many applications requiring high-resolution, high-precision data will require favourable flow conditions. However, for other potential applications, surveying submerged bridge structures, for example, the additional error introduced under normal flow conditions may be acceptable for the purposes of the survey. Likewise, Fuller and Basher (2012) reported annual bed-level changes of up to ±2 m, which would be easily identified using through-water TLS. Errors generally <10 mm have been reported in this study. This is comparable with or even better than results obtained for optical–empirical depth models (Westaway *et al*., 2003; Williams *et al*., 2011) but at a much finer spatial resolution.

Field tests demonstrated that obtaining approximate reach-scale bathymetry is possible using through-water TLS, although submerged points are obtained with lower precision than sub-aerial TLS surveys. In many situations, where deep and turbid channel flows are observed, the method is unsuitable. However, where the channel is made up of marginally or partially submerged surfaces, acceptable reach-scale bathymetry can be obtained (Figure 11). Point density is dependent upon surface flow conditions, bottom reflectance and range. Specular reflections may preclude the survey of still-water surfaces at high angles of incidence, and white water prevents laser penetration. Nevertheless, although point accuracy and precision are less than those for total station or differential global positioning system survey, higher-resolution bathymetry can be obtained with large efficiency savings and without the financial cost of airborne bathymetric lidar, enabling regular monitoring studies. Such surveys provide essential information for mitigation and restoration projects or evaluations of potential riverine ecological impacts. In addition, through-water TLS datasets can be readily nested within larger-scale bathymetric maps of river corridors to provide multi-scalar information.

CONCLUDING REMARKS

Through-water TLS provides fully three-dimensional bathymetry at high accuracy, precision and resolution at the patch scale and is capable of surveying shallow river reaches with reasonable point accuracy (<10 mm), precision (RSEV~20 mm) and resolution (from a few points per square metre to almost 10 points per square centimetre). This paper has evaluated through-water TLS under a range of flow and turbidity conditions and presented the first reach-scale through-water TLS-derived bathymetric map. Specific limits relating to flow regime, water depth and water turbidity have been identified; however, accurate and precise surveys (<10-mm error) are possible under conditions that might be encountered in many upland rivers during low flows. Identified limits are specific to Leica ScanStation green-wavelength TLS equipment, although the through-water correction could be applied using other green-wavelength TLS devices. Through-water TLS may be useful in certain laboratory settings where water surface elevation can be estimated and draining overlying water is either impracticable or time-consuming. Most significantly, through-water TLS can provide topographic data of marginally and partially inundated areas on the river margins, thereby bridging the gap between exposed surfaces regularly surveyed using TLS and deeply submerged surfaces with sufficient clearance depth for more standard bathymetric surveying equipment. The resulting high-resolution bathymetric survey provides information on bed topography, roughness and heterogeneity in fluvial environments of use for hydrological, geomorphological and ecological applications and can inform the activities of river restoration and management.

ACKNOWLEDGEMENTS

The authors thank Aberystwyth University for funding this research and James Brasington for thoughtful discussions of the necessary refraction correction. The second author has benefitted from a Ramon y Cajal Fellowship (RYC-2010-06264), funded by the Spanish Ministry of Science and Innovation during the preparation of this manuscript. Field experiments were designed to support and validate the experimental approach presented in the research project MorphSed (CGL2012-36394, funded by the Spanish Ministry of Economy and Competitiveness). Field experiments were conducted in the framework of a sediment transport mobility project requested by Endesa Generación SA. We thank Ramon J. Batalla and Alvaro Tena at the University of Lleida for support in the field and two anonymous reviewers who improved this manuscript.

REFERENCES

Ashmore P, Church M. 1998. Sediment transport and river morphology: a paradigm for study. In Gravel Bed Rivers in the Environment, Klingeman PC, Beschta RL, Komar PD, Bradley JB (eds). Water Resources Publications: Highlands Ranch, CO; 115–148.

Bailly J-S, Le Coarer Y, Languille P, Stigermark C-J, Allouis T. 2010. Geostatistical estimations of bathymetric lidar errors on rivers. *Earth Surface Processes and Landforms* **35**: 1199–1210. doi: 10.1002/esp.1991.

Brasington J, Rumsby BT, McVey RA. 2000. Monitoring and modelling morphological change in a braided gravel-bed river using high-resolution GPS-based survey. *Earth Surface Processes and Landforms* **25**: 973–990.

Brasington J, Langham J, Rumsby B. 2003. Methodological sensitivity of morphometric estimates of coarse fluvial sediment transport. *Geomorphology* **53**: 299–316.

Brasington J, Vericat DV, Rychkov I. 2012. Modelling river bed morphology, roughness and surface sedimentology using high resolution terrestrial laser scanning. *Water Resources Research* **48**: W11519. doi: 10.1029/2012WR012223.

Buffin-Bélanger T, Reid I, Rice S, Chandler J, Lancaster J. 2003. A casting procedure for reproducing coarse-grained sedimentary surfaces. *Earth Surface Processes and Landforms* **28**: 787–796.

Butler JB, Lane SN, Chandler JH. 1998. Assessment of DEM quality for characterizing surface roughness using close range digital photogrammetry. *The Photogrammetric Record* **16**: 271–291.

Butler JB, Lane SN, Chandler JH. 2002. Through-water close-range digital photogrammetry in flume and field experiments. *The Photogrammetric Record* **17**: 419–439.

Carbonneau PE, Lane SN, Bergeron N. 2006. Feature based image processing methods applied to bathymetric measurements from airborne remote sensing in fluvial environments. *Earth Surface Processes and Landforms* **31**: 1413–1423.

Daimon M, Masumura A. 2007. Measurement of the refractive index of distilled water from the near-infrared region to the ultraviolet region. *Applied Optics* **46**: 3811–3820. doi:10.1364/AO.46.003811.

Fewtrell TJ, Duncan A, Sampson CC, Neal JC, Bates PD. 2011. Benchmarking urban flood models of varying complexity and scale using high resolution terrestrial lidar data. *Physics and Chemistry of the Earth* **36**: 281–291.

Fonstad MA, Marcus WA. 2005. Remote sensing of stream depths with hydraulically assisted bathymetry (HAB) models. *Geomorphology* **72**: 107–120.

Fuller IC, Basher, LR. 2012. Riverbed digital elevation models as a tool for holistic river management: Motueka River, Nelson, New Zealand. *River Research and Applications*. doi: 10.1002/rra.2555.

Gao J. 2009. Bathymetric mapping by means of remote sensing: methods, accuracy and limitations. *Progress in Physical Geography* **33**: 103–116.

Gibbins CN, Batalla RJ, Vericat D. 2010. Invertebrate drift and benthic exhaustion during disturbance: response of mayflies (Ephemeroptera) to increasing shear stress and river-bed instability. *River Research and Applications* **26**: 499–511.

Grayson R, Holden J. 2012. Continuous measurement of spectrophotometric absorbance in peatland streamwater in northern England: implications for understanding fluvial carbon fluxes. *Hydrological Processes* **26**: 27–39.

Guenther GC, Cunningham AG, LaRocque PE, Reid DJ. 2000. Meeting the accuracy challenge in airborne lidar bathymetry. *Proceedings of EARSeL-SIG Workshop LiDAR No. 1*, Dresden, 16–17 June.

Hardy RJ, Lane SN, Lawless MR, Best JL, Elloitt AH, Ingham DB. 2005. Development and testing of a numerical code for treatment of complex river channel topography in three-dimensional CFD models with structured grids. *Journal of Hydraulic Research* **43**: 468–480.

Hauer C, Madlburger G, Habersack H. 2009. Hydraulically related hydromorphological units: description based on a new conceptual mesohabitat evaluation model (MEM) using lidar data as geometric input. *River Research and Applications* **25**: 29–47.

Hauer C, Unfer G, Tritthart M, Formann E, Habersack H. 2011. Variability of mesohabitat characteristics in riffle-pool reaches: testing an integrative evaluation concept (FGC) for MEM-application. *River Research and Applications* **27**: 403–430.

Hauer C, Unfer G, Graf W, Leitner P, Zeiringer B, Habersack H. 2012. Hydro-morphologically related variance in benthic drift and its importance for numerical habitat modelling. *Hydrobiologia* **683**: 83–108.

Hilldale RC, Raff D. 2008. Assessing the ability of airborne lidar to map river bathymetry. *Earth Surface Processes and Landforms* **33**: 773–783.

Hodge R, Brasington J, Richards K. 2009. In situ characterisation of grain-scale fluvial morphology using terrestrial laser scanning. *Earth Surface Processes and Landforms* **34**: 954–968.

Höfle B, Rutzinger M. 2011. Topographic airborne lidar in geomorphology: a technological perspective. *Zeitschrift für Geomorphologie* **55**: 1–29.

James WF, Best EPH, Barko JW. 2002. Suspended sediment dynamics and light attenuation characteristics in Peoria Lake, Illinois: can submersed macrophyte communities improve water quality in this shallow system? Aquatic Plant Control Research Program, U.S. Army Corps of Engineers, ERDC/EL TR-02-2.

Karlsson J, Byström P, Ask J, Ask P, Persson L, Jansson M. 2009. Light limitation of nutrient-poor lake ecosystems. *Nature* **460**: 506–509.

Lacey RWJ, Roy A. 2008. The spatial characterisation of turbulence around large roughness elements in a gravel-bed river. *Geomorphology* **102**: 542–553.

Lancaster J, Buffin-Bélanger T, Reid I, Rice SP. 2006. Flow- and substratum-mediated movement by a stream insect. *Freshwater Biology* **51**: 1053–1069.

Lane SN. 2000. The measurement of river channel morphology using digital photogrammetry. *The Photogrammetric Record* **16**: 937–961.

Lane SN, Westaway RM, Hicks M. 2003. Estimation of erosion and deposition volumes in a large, gravel-bed, braided river using synoptic remote sensing. *Earth Surface Processes and Landforms* **28**: 249–271.

Lane SN, Hardy RJ, Elliott L, Ingham DB. 2004. Numerical modeling of flow processes over gravelly surfaces using structured grids and a numerical porosity treatment. *Water Resources Research* **40**: W01302. doi:10.1029/2002WR001934.

Legleiter CJ, Roberts DA, Lawrence RL. 2009. Spectrally based remote sensing of river bathymetry. *Earth Surface Processes and Landforms* **34**: 1039–1059.

Legout C, Darboux F, Nédélec Y, Hauet A, Esteves M, Renaux B, Denis H, Cordier S. 2012. High spatial resolution mapping of surface velocities and depths for shallow overland flow. *Earth Surface Processes and Landforms* **37**: 984–993. doi: 10.1002/esp.3220.

Leica Geosystems. 2007. Leica ScanStation. Available from http://www.surveyequipment.com/PDFs/leica-scanstation-datasheet.pdf [15 June 2012].

Leica Geosystems. 2011. Leica ScanStation C10. Available from http://hds.leica-geosystems.com/downloads123/hds/hds/ScanStation%20C10/brochures-datasheet/Leica_ScanStation_C10_DS_en.pdf [06 September 2012].

Lyzenga DR. 1981. Remote sensing of bottom reflectance and water attenuation parameters in shallow water using aircraft and Landsat data. *International Journal of Remote Sensing* **2**: 71–82.

Mallet C, Bretar F. 2009. Full-waveform topographic lidar: state-of-the-art. *ISPRS Journal of Photogrammetry and Remote Sensing* **64**: 1–16.

Mandlburger G, Hauer C, Höfle B, Habersack H, Pfeifer N. 2009. Optimisation of lidar derived terrain models for river flow modelling. *Hydrology and Earth System Sciences* **13**: 1453–1466.

McKean J, Nagel D, Tonina D, Bailey P, Wright CW, Bohn C, Nayegandhi A. 2009. Remote sensing of channels and riparian zones with a narrow-bean aquatic-terrestrial lidar. *Remote Sensing* **1**: 1065–1096.

Milan DJ, Heritage GL, Hetherington D. 2007. Application of a 3D laser scanner in the assessment of erosion and deposition volumes and channel change in a proglacial river. *Earth Surface Processes and Landforms* **32**: 1657–1674.

Milan DJ, Heritage GL, Large ARG, Entwistle NS. 2010. Mapping hydraulic biotopes using terrestrial laser scan data of water surface properties. *Earth Surface Processes and Landforms* **35**: 918–931.

Milan DJ, Heritage GL, Large ARG, Fuller IC. 2011. Filtering spatial error from DEMs: implications for morphological change estimation. *Geomorphology* **125**: 160–171.

Milne JA, Sear D. 1997. Modelling river channel topography using GIS. *International Journal of Geographical Information Science* **11**: 499–519.

PerkinElmer. 2008. Lambda XLS/XLS + User's Guide. UV–VIS Spectroscopy. PerkinElmer: Beaconsfield.

Petit F, Gob F, Houbrechts G, Assani AA. 2005. Critical specific stream power in gravel-bed rivers. *Geomorphology* **69**: 92–101.

Raineault NA, Trembanis AC, Miller DC. 2012. Mapping benthic habitats in Delaware Bay and the coastal Atlantic: acoustic techniques provide greater coverage and high resolution in complex, shallow-water environments. *Estuaries and Coasts* **35**: 682–699.

Rice SP, Lancaster J, Kemp P. 2010. Experimentation at the interface of fluvial geomorphology, stream ecology and hydraulic engineering and the development of an effective, interdisciplinary river science. *Earth Surface Processes and Landforms* **35**: 64–77.

Rychkov I, Brasington J, Vericat D. 2012. Computational and methodological aspects of terrestrial surface analysis based on point clouds. *Computers and Geosciences* **42**: 64–70.

Sampson CC, Fewtrell TJ, Duncan A, Shaad K, Horritt MS, Bates PD. 2012. Use of terrestrial laser scanning data to drive decimetric resolution urban inundation models. *Advances in Water Resources* **41**: 1–17.

Smith MW, Cox NJ, Bracken LJ. 2007. Applying flow resistance equations to overland flows. *Progress in Physical Geography* **31**: 363–387.

Smith MW, Vericat D, Gibbins CN. 2012. Through-water terrestrial laser scanning of gravel beds at the patch scale. *Earth Surface Processes and Landforms* **37**: 411–421.

Vericat D, Batalla RJ. 2010. Sediment transport from continuous monitoring in a perennial Mediterranean stream. *Catena* **82**: 77–86.

Vetter M, Höfle B, Mandlburger G, Rutzinger M. 2011. Estimating changes of riverine landscapes and riverbeds by using airborne lidar data and river cross-sections. *Zeitschrift für Geomorphologie* **55**: 51–65.

Wang C-K, Philpot WD. 2007. Using airborne bathymetric lidar to detect bottom type variation in shallow waters. *Remote Sensing of Environment* **106**: 123–135.

Westaway RM, Lane SN, Hicks DM. 2000. The development of an automated correction procedure for digital photogrammetry for the study of wide, shallow, gravel-bed rivers. *Earth Surface Processes and Landforms* **25**: 209–226.

Westaway RM, Lane SN, Hicks DM. 2003. Remote survey of large-scale braided, gravel-bed rivers using digital photogrammetry and image analysis. *International Journal of Remote Sensing* **24**: 795–815.

Wheaton JM, Brasington J, Darby SE, Sear DA. 2010. Accounting for uncertainty in DEMs from repeat topographic surveys: improved sediment budgets. *Earth Surface Processes and Landforms* **35**: 136–156.

Williams RD, Brasington J, Vericat D, Hicks DM, Labrosse F, Neal MN. 2011. Monitoring braided river change using terrestrial laser scanning and optical bathymetric mapping. In Geomorphological Mapping, Smith M, Paron P, Griffiths J (eds). Elsevier: Oxford; 507–531.

Winterbottom SJ, Gilvear DJ. 1997. Quantification of channel bed morphology in gravel-bed rivers using airborne multispectral imagery and aerial photography. *Regulated Rivers: Research & Management* **13**: 489–499.

DOI: 10.1002/rra